Nano Research

Open Access

Research Article

A mechanical reinforced and antifreezing polyacrylate hydrogel electrolyte for high-performance zinc-ion batteries

Zili Zhang[1], Ruolin Wang[1], Hongfei Lu[1], Di Zhang[1], Yu Zhao[1], Jing Xu[1], Bin Sun[1], Zhi-Min Dang[1,2], and Yang Jin[1]✉

[1] *School of Electrical and Information Engineering, Zheng Zhou University, Zhengzhou 450001, China*
[2] *State Key Laboratory of Power System Operation and Control, Department of Electrical Engineering, Tsinghua University, Beijing 100084, China*

Cite this article: *Nano Research*, **2025**, *18*, 94906999. https://doi.org/10.26599/NR.2025.94906999

ABSTRACT: The operation of aqueous zinc-ion batteries in flexible energy storage field is plagued by the uncontrollable growth of Zn-dendrite and inevitable freeze of water below 0 °C. Therefore, it is necessary to design a hydrogel electrolyte with good mechanical property and freezing resistance to uniform the Zn-deposition and resist flexibility loss at low temperature. We find that the mechanical property (strength and toughness) of hydrogel electrolyte has a significant impact on the suppression of dendrite growth and the uniform deposition of zinc ions. Herein, a polyacrylate hydrogel is prepared in one step by ultraviolet (UV) curing method with $Zn(CF_3SO_3)_2$ salt and polyvinyl alcohol (PVA) addition to increase the antifreezing ability and mechanical properties. The adsorption of water molecules by 2-hydroxyethyl acrylate (HEA) and PVA reduces the freezing point of the hydrogel, which is beneficial for enhancing the electrochemical stability at low temperature. On this basis, the Zn-symmetrical battery with hydrogel electrolyte has a long lifespan of 4710 h at 0.5 mA·cm^{-2} and 0.5 mAh·cm^{-2} at room temperature. Furthermore, the hydrogel electrolyte exhibits an outstanding stability at low temperature of −20 °C, the lifespan of symmetrical battery reaches to 4000 h at 0.5 mA·cm^{-2} and 0.5 mAh·cm^{-2}. The assembled full cell with $NaV_3O_8·1.5H_2O$ (NVO) cathode and hydrogel electrolyte possesses a high capacity retention ratio of 77% after 10,000 cycles at −20 °C. The flexible cell can power light-emitting diode (LED) lamp under bending, warping and cutting without liquid leakage and an electronic watch at the operating temperature of −20 °C.

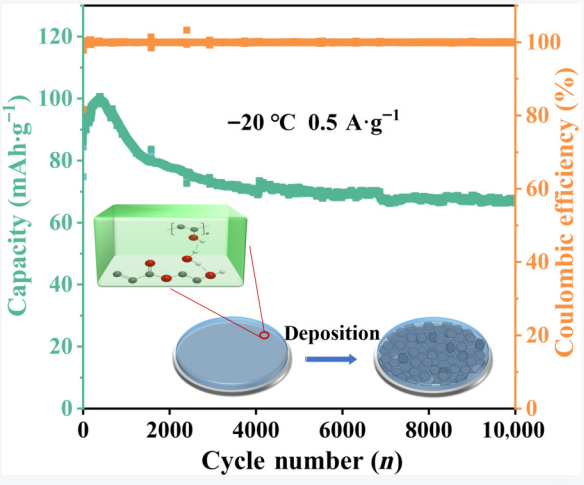

KEYWORDS: zinc ion battery, hydrogel electrolyte, mechanical enhancement, freezing resistance

1 Introduction

In recent years, flexible and wearable electronic devices, such as smart clothing, implantable medical devices, artificial electronic skin and electronic bracelets, have been attracting significant interests. As a result, the development of matching flexible energy storage batteries has become more and more urgent [1–3]. Traditional lithium-ion batteries are rigid. There is a risk of leakage from the liquid electrolyte when bent or folded, which is easy to degrade the electrochemical performance and trigger serious safety issues [4–6]. Aqueous zinc-ion batteries (ZIBs) show great potential in flexible energy storage field due to their high theoretical energy density, high safety and environmental friendliness [7–9]. However, common sandwich-stacked structural batteries are susceptible to electrode-separator detachment during deformation and degeneration in electrochemical performance, which cannot be qualified as flexible energy storage devices [10–12]. Hydrogel, a three-dimensional (3D) network formed by crosslinking of hydrophilic polymer chains, has the ability to absorb a significant amount of water and maintain its original three-dimensional structure, in which solutes can diffuse or permeate [13]. Therefore, hydrogel can act as quasi-solid-state electrolytes and possess an anti-deformation ability and high ion conductivity, making it a promising candidate of semi-solid electrolytes for flexible ZIBs [14–16]. However, the hydrogel with full water absorption usually has a poor mechanical property, resulting in inability to resist Zn-dendrite growth during the electrochemical cycling [17–19]. On the

Received: June 19, 2024; **Revised:** August 6, 2024
Accepted: August 23, 2024

✉Address correspondence to yangjin@zzu.edu.cn

other hand, the hydrogel will inevitably freeze as the temperature drops below zero due to the large amount of contained water, which severely limits the mobility of ions and the flexibility of the hydrogel electrolyte at low temperatures [20–22].

Great efforts have been made to increase the mechanical property of hydrogel electrolyte, such as grafting rigid group onto the polymer chain, adding hard polymer chain into the cross-linked network and using multiple crosslinking method to construct strong polymer network [23–25]. For lowering the freezing point of hydrogel electrolytes, the break of hydrogen-bonds between water molecules is essential for impeding freezing process of water [21, 26]. Recent studies showed that hybrid liquid (glycol-water, dimethyl sulfoxide-water), high concentration salt solution ($ZnCl_2$, ZnTFSI (TFSI: bis((trifluoromethyl)sulfonyl)azanide)), antifreeze agent (glycerinum), zinc salt ($Zn(ClO_4)_2$, $ZnBF_4$) on the right of Hofmeister's sequence and rigid group (–OH, –F) on the polymer chain were generally used to lower the freezing point of water and inhibit flexibility loss of the hydrogel [27–30]. The polar groups can absorb H_2O molecules by forming new hydrogen bonds instead of that between water molecules. The anchoring effect of water molecules can lower the freezing point of water, optimize the solvation shell of Zn-ions, broaden the electrochemical window, which is beneficial to achieve stable operation in a wide temperature range [22, 31]. Although these strategies have been proven to be effective, the fabrication of hydrogel usually requires a complex process. The pre-synthetic polymer networks soaked in aqueous solution to absorb water and swell for tens of hours. The immoderate swelling may lead to the uncontrol of hydrogel components and decline the mechanical property. In recent years, the preparation of hydrogel electrolytes by ultraviolet (UV) curing method has been receiving increasing attention. UV curing can quickly prepare the film hydrogels and realize the precise control of their components, which is beneficial to adjust the electrochemical and mechanical properties [32, 33].

In this work, we design and fabricate a 2-hydroxyethyl acrylate (HEA)/poly (ethylene glycol) diacrylate (PEGDA)/polyvinyl alcohol (PVA)/$Zn(CF_3SO_3)_2$ multicomponent hydrogel electrolyte (defined as HP-P) with good mechanical properties in one step by a simple UV curing method. This one step method effectively increases the flatness and evenness of the hydrogel and realizes the precise control of the components. According to the density functional theory (DFT) calculation, H_2O molecules are more inclined to bind with HEA and PVA and form strong hydrogen bonds, which inhibits hydrogen evolution reaction and improves water retention. Moreover, the break between H_2O molecules inhibits the formation of ice crystals, making the hydrogel electrolyte have an excellent reversibility at low temperature. The zinc-symmetric battery assembled with HP-P electrolyte achieved an ultralong cycle life of over 4700 h at room temperature of 25 °C and 4000 h at low temperature of −20 °C under plating/stripping capacity of 0.5 mAh·cm^{-2} and current density of 0.5 mA·cm^{-2}. The resulting full cells based on NaV_3O_8·1.5H_2O (NVO) cathode and HP-P electrolyte achieve a capacity of 66.4 mAh·g^{-1} and capacity retention ratio 77% after 10,000 cycles at −20 °C.

2 Experimental

2.1 Materials

HEA, PEGDA, PVA, 2-hydroxy-4'-(2-hydroxyethoxy)-2-methylpropiophenone (HHMP), NaCl and V_2O_5 were purchased from Shanghai Aladdin Biochemical Technology Co., Ltd. Zinc trifluoromethanesulfonate ($Zn(CF_3SO_3)_2$) was purchased from Shanghai Macklin Biochemical Co. Ltd. Ultrapure water was obtained from the Milli-Q water purification system.

2.2 Fabrication of HP-P hydrogel electrolyte

According to the component ratios in Table 1, HEA, PEGDA, PVA, $Zn(CF_3SO_3)_2$ and HHMP were dropped in deionized water under magnetic stirring, where PEGDA is the cross-linking agent, HEA is the monomer, HHMP is used as a photoinitiator for UV curing. After being stirred for 6 h and debubbling in vacuum oven for 2 h, the solution was injected into a homemade vessel with thickness of 0.4 mm and cured in an light-emitting diode (LED) cold light curing chamber (aventk XM201 UVLED) for 1 min. After cooling to room temperature, the hydrogel film is removed from the homemade vessel and sliced into round pieces used as electrolyte.

Table 1 Formulations (parts of weight) of the hydrogels

Hydrogels	HEA	PEGDA	PVA	H_2O
HP	2.4	0.27	0	3
HP-P	2.4	0.27	0.3	3
HP-P2	2.4	0.27	0.6	3
HP-P3	2.4	0.27	0.9	3
H_{99}P-P	2.4	0.024	0.3	3
H_{999}P-P	2.4	0.0024	0.6	3

2.3 Material characterization

The scanning electron microscopy (SEM) images were captured using the ZEISS Auriga SEM/FIB Crossbeam system. Infrared (IR) spectra were measured on an IR spectrometer (IRTracer-100) in the 600–4000 cm^{-1} wavenumber range. Mechanical tensile measurements were performed using an electronic universal testing machine (AGS-X-100N SHIMADZU) with a tensile speed of 50 mm·min^{-1} until the samples (0.2 mm × 10 mm × 40 mm) broke. The phases of the samples were verified by XRD using a Rigaku D/max-RB12 X-ray diffractometer with Cu Kα radiation. 3D confocal laser scanning images were tested on a Zetasizer Nano ZS (Malvern Instruments, Southborough, MA) equipped with a laser with a wavelength of 633 nm at a 173° scattering angle.

2.4 Fabrication of NVO nanobelts and NVO cathode

The NVO nanobelts were prepared the same as the previously reported method [34]. 1 g of V_2O_5 powder was added into 15 mL of NaCl aqueous solution (2 M). After stirring for 96 h at 30 °C, the suspension was washed with deionized water several times. Finally, the black-red product was obtained by freeze-drying and named as NVO. The NVO nanobelts were ground using an agate grinding bowl for 15 min to prepare cathode for ZIBs. The NVO nanobelts (70 wt.%), acetylene black (20 wt.%) and poly(vinylidene fluoride) binder (10 wt.%) were dispersed in 0.5 mL of N-methylpyrrolidone and stirred for 10 min to form slurry. The slurries were doctor-bladed onto a stainless steel (SS) mesh (400 mesh) and dried by freeze-drying. Use a microtome for the slices and cut them into discs with a diameter of 11 mm. The mass loading of the NVO nanobelts in the cathode foil is 2.5–3 mg·cm^{-2}.

2.5 Electrochemical measurements

The zinc foil was polished with 2000 mesh sandpaper to remove the

surface oxide layer and pressed into Zn-sheet with a diameter of 12 mm by a tablet press, followed by cleaning with anhydrous ethanol in ultrasonic machine. The button battery case of CR2016 is cleaned with anhydrous ethanol in ultrasonic cleaning machine as well. From bottom to top, the assembly sequence of symmetric cell is the positive case, Zn-electrode foil, HP-P electrolyte, Zn-electrode foil, gasket and negative case, named as Zn||HP-P. The symmetric cell with aqueous electrolyte is assembled with glass fiber separator instead of HP-P and addition of 70 μL aqueous solution (2 M $Zn(CF_3SO_3)_2$), named as Zn||AE (AE: aqueous electrolyte). The assembly sequence of the full cell is the positive case, cathode foil, HP-P electrolyte, anode foil, gasket and negative case. The seal pressure is approximately 50 $kg·cm^{-2}$. The anode and cathode of pouch battery are both of rectangular with dimensions of 2 cm in width and 6 cm in length and a tab of 3 cm in length is left at the narrow end. The effective area is 12 cm^2. The cathode has a thickness of 0.1 mm and a weight of 0.3 g. The anode is a polished zinc foil with a thickness of about 0.1 mm and a weight of about 1 g. The HP-P hydrogel electrolyte, with a thickness of 0.4 mm, is cut into a rectangular shape with dimensions of 2 * 6 cm, weighing approximately 0.6 g. The cathode, electrolyte and anode are stacked in sequence, placed into an aluminum foil bag and sealed with a vacuum sealer to complete the assembly of the pouch cell. All coin cells are tested on the Lanhe battery test system in calorstat (−20–60 °C) through the air conditioning. Cyclic voltammetry (CV) measurements with a scan rate of 0.5 $mV·s^{-1}$, linear sweep voltammetry (LSV), Tafel kinetics testing and chronoamperometry (CA) use Bio-Logic VSP Five-channel Electrochemical Workstations.

3 Results and discussion

3.1 Characterization of the hydrogel electrolyte

To synthesize the HP-P hydrogel electrolyte, HEA monomer and PEGDA crosslinking agent are used to form the hydrogel framework through the UV curing method in the presence of PVA, water and $Zn(CF_3SO_3)_2$ (Fig. 1(a)). The SEM image shows the morphology of HP-P hydroel after freeze-drying. The diameter of interconnected pores is 0.1–0.7 μm, which increases the water

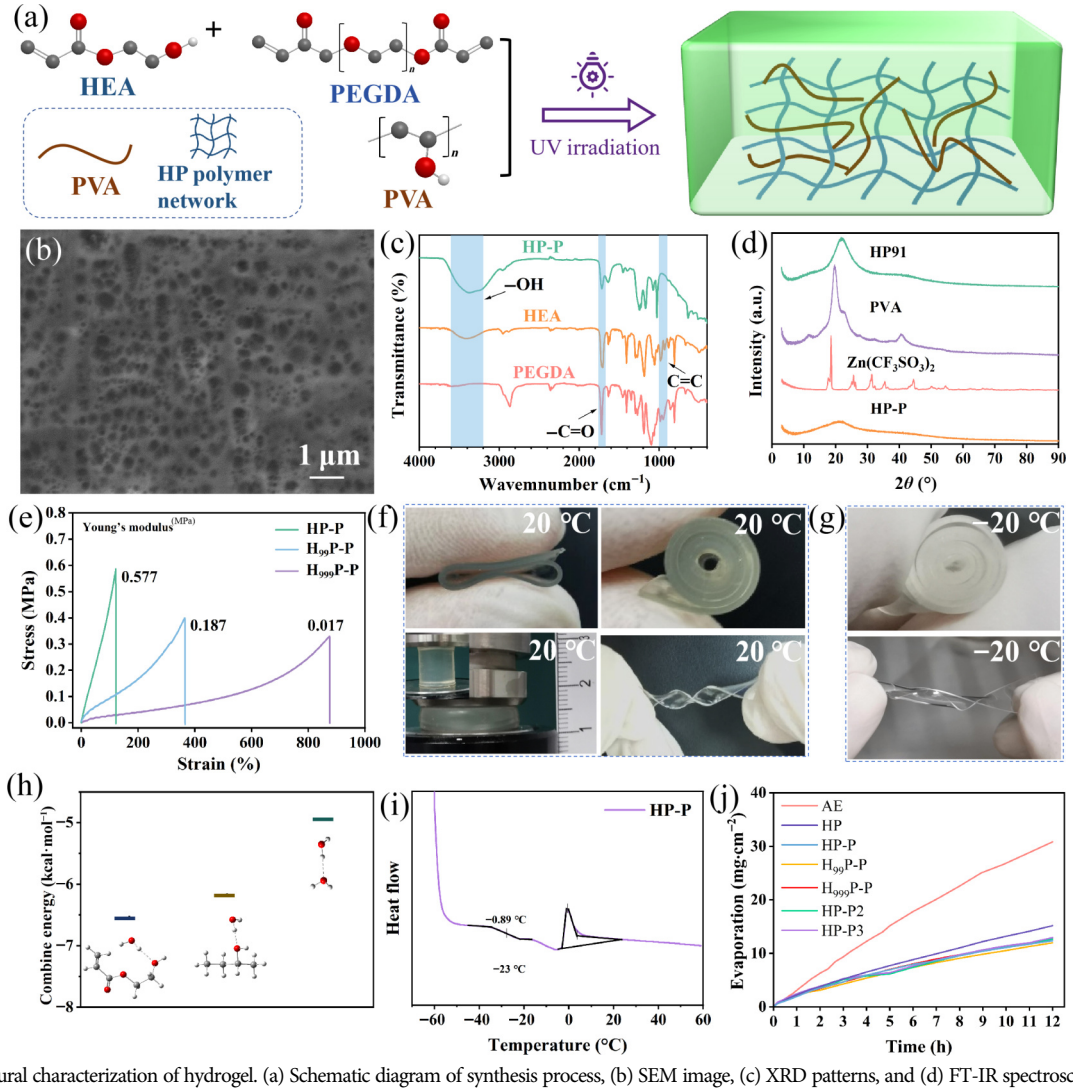

Figure 1 Structural characterization of hydrogel. (a) Schematic diagram of synthesis process, (b) SEM image, (c) XRD patterns, and (d) FT-IR spectroscopy of the HP-P electrolyte. (e) Stress–strain curves of HP-P and HP hydrogel. Optical photo of the HP-P hydrogel after (f) folded in half, curled, rotated, compressed (70%) at 25 °C, (g) bended and curled at −25 °C. (h) The formation energy from DFT calculations. (i) Differential scanning calorimetry (DSC) curve of the HP-P hydrogel. (j) The weight retention of the hydrogels and Zn-salt solution.

retention and provides fast Zn^{2+} transport paths (Fig. 1(b)). The crystallinity of the HP-P hydrogel was characterized by X-ray diffraction (XRD) as shown in Fig. 1(c). The XRD patterns clearly show the HP-P hydrogel is in amorphous state, indicating that $Zn(CF_3SO_3)_2$ dissolved in water to conduct Zn-ion and PVA dispersed in the polymer matrix to increase plasticity. Figure 1(d) displays the Fourier transform (FT)-IR spectroscopy of HP-P, HEA and PEGDA, respectively. The broad band between 3600–3200 cm^{-1} is caused by the O–H stretching vibration provided by PVA, HEA and H_2O [35]. The peeks of C=C bond at 990 and 910 cm^{-1} in HEA and PEGDA were disappeared in HP-P hydrogel, illustrating the accomplishment of cross-linking reaction between HEA and PEGDA.

Reducing the amount of PEGDA can effectively reduce the modulus and increase the elongation at break of the hydrogel, which was revealed by uniaxial tensile testing displayed in Fig. 1(e). The elongation at break of the H_{999}P-P hydrogel reaches to ~ 900%, but the strength reduces to 0.017 MPa, as the content of PEGDA is reduced to a ratio of 999:1 with HEA. On the other hand, the addition of PVA can also increase the flexibility of the hydrogel. With the increase of PVA content, the flexibility increases (elongation at break rises from 30% to 164%), but the strength reduces (the Young's modulus decreases from 0.703 to 0.289 MPa, Fig. S1 in the Electronic Supplementary Material (ESM)). The HP-P hydrogel can be repeatedly folded in half, curled, rotated, compressed (70%) at room temperature, which shows a good flexibility, laying a good foundation for the preparation of flexible batteries (Fig. 1(f) and Video S1 in the ESM). On the contrary, the HP hydrogel can be easily broken during warping or buckling (Fig. S2 in the ESM). More importantly, the HP-P hydrogel has a good flexibility at low temperature (Fig. 1(g)). There is no physical crack or breakage after bending and curling, making it possible to achieve good electrochemical performance at low temperature of –20 °C.

The combine energy between molecules was calculated by DFT methods to explore the effect of polar functional groups in HEA and PVA on breaking hydrogen bonds between water molecules (Fig. 1(h)). The results show that the formation energy of HEA-H_2O and PVA-H_2O is lower than H_2O-H_2O, which suggests that the H_2O molecules prefer to bond with HEA and PVA. The freezing resistance and water retention of hydrogel electrolyte get promoted as shown in Figs. 1(i) and 1(j), respectively. It is interesting that the HP hydrogel without PVA shows the worst water retention of all the hydrogels (but still better than Zn-salt solution), which further verifies the effect of PVA on the water-holding capacity of hydrogel electrolyte.

3.2 Electrochemical performance regulation mechanism of hydrogel electrolyte

In order to clarify the influence of mechanical property on the uniform Zn-deposition and the suppression of dendrite growth, *in-situ* optical microscopy testing was used to discover the dynamic deposition evolution of Zn anode in hydrogel electrolyte with different modulus at a current density of 10 $mA{\cdot}cm^{-2}$. As shown in Fig. 2(a), the Zn-dendrite starts to occur on the Zn anode with H_{999}P-P hydrogel electrolyte after deposition for 5 min and rapidly grows up within 10 min. On the contrary, the deposition on Zn

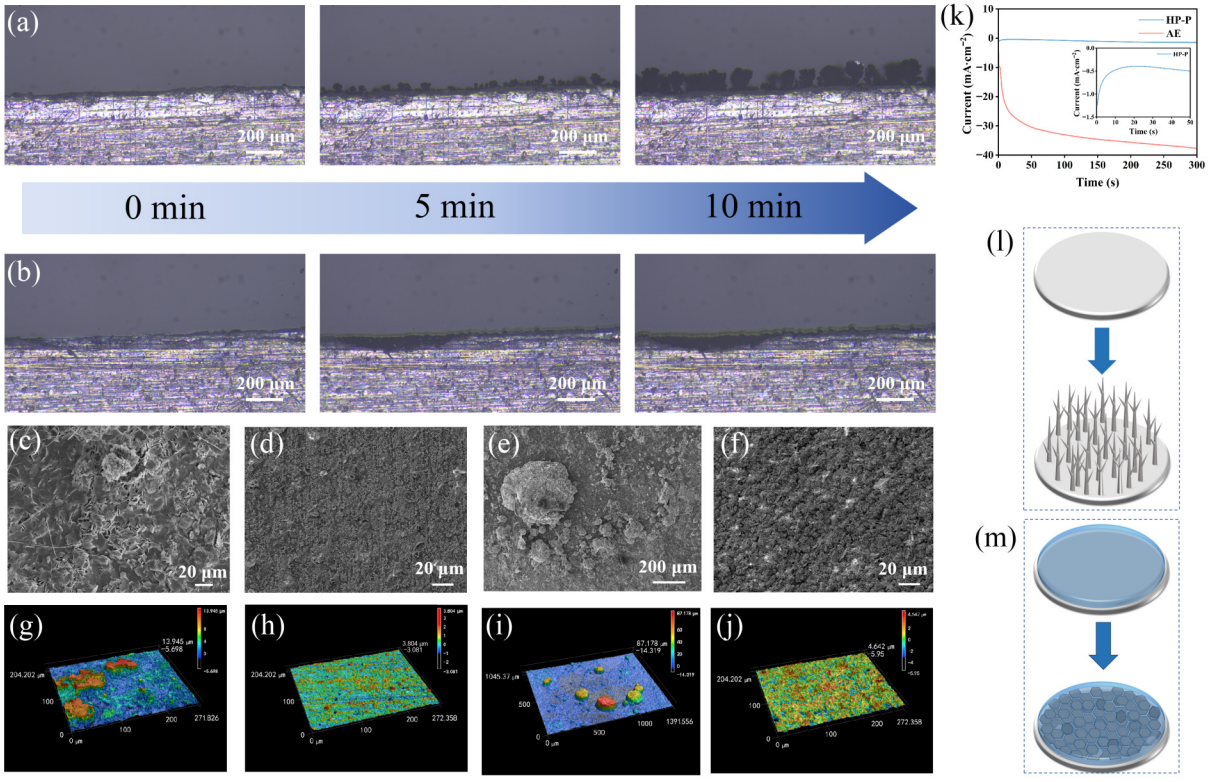

Figure 2 *In/ex-situ* characterization of Zn anode during electrochemical cycles. *In-situ* optical microscopy images of Zn foil during the electroplating of Zn||Zn symmetric cells in (a) H_{999}P-P and (b) HP-P hydrogel electrolyte. SEM images of Zn anode after 1 cycle with (c) AE and (d) HP-P electrolyte, 50 cycles with (e) AE and (f) HP-P electrolyte. 3D confocal laser scanning images of Zn anode after of Zn anode after 1 cycle with (g) AE and (h) HP-P electrolyte, 50 cycles with (i) AE and (j) HP-P electrolyte. (k) Chronoamperograms of Zn||HP-P and Zn||AE symmetrical cells. Schematic illustration on a mechanism of Zn deposition in (l) AE electrolyte and (m) HP-P hydrogel electrolyte.

anode with HP-P hydrogel electrolyte is relative uniform without distinct dendrites after 10 min (Fig. 2(b)), which strongly proves that the modulus of the hydrogel can effectively suppress dendrite growth.

To further understand the mechanism of HP-P electrolyte affecting the cycle stability, the evolution of Zn electrode surface was represented by SEM, confocal laser scanning microscopy (CLSM) and digital photograph of different cycling number at current density of 0.5 mA·cm^{-2} and constant plating/stripping capacity of 0.5 mAh·cm^{-2} (Figs. 2(c)–2(j) and Figs. S3 and S4 in the ESM). The SEM images in Fig. 2(c) and Fig. S5(a) in the ESM display the surface morphology of Zn||AE anode after one stripping/plating cycle. Obviously, a lot of cluttered flakes formed on the surface of Zn anode, resulting in a bumpy Zn surface. The growth of Zn dendrites would exacerbate the uneven deposition and serious hydrogen evolution reaction [36, 37]. By contrast, the surface of Zn||HP-P anode was dense and flat (Fig. 2(d) and Fig. S5(b) in the ESM), demonstrating its good adjusting ability of homogeneous Zn deposition. After 50 cycles, a mass of irregular blocks (made of fiberglass and plating Zn) with different sizes grown on the surface of Zn||AE anode, leading to a more rugged surface and the formation of "dead Zn" (Fig. 2(e) and Fig. S5(c) in the ESM). The blocks on the surface of Zn||AE anode grown bigger till to penetrate separators and short circuit after 100 cycles (Figs. S3(a) and S5(e) in the ESM). As for Zn||HP-P anode, closely packed Zn nanosheets were uniformly deposited on the surface of Zn anode without any abnormal local protrusion after 50 and 100 cycles (Fig. 2(f) and Figs. S3(b), S5(d) and S5(f) in the ESM), which strongly proves the ability to uniform Zn-deposition and inhibit Zn-dendrite growth of HP-P electrolyte.

The *ex-situ* CLSM images and the surface roughness of Zn||AE and Zn||HP-P anode are shown in Figs. 2(g)–2(j) and Figs. S6 and S7 in the ESM. As the increase of cycling number, the surface of Zn-AE anode becomes rougher (15 to 122 μm of drop from 1 to 100 cycles), which would aggravate the growth of Zn-dendrite [22, 38]. However, the roughness of Zn||HP-P anode changes negligibly after 100 cycles (7.4 μm of drop), which matches nicely with the SEM images above and further demonstrates the ability for optimizing Zn stripping/planting and increasing the longterm cycling stability of HP-P electrolyte.

To comprehend the nucleation and deposition mechanism of Zn^{2+}, CA was measured at a constant overpotential of −150 mV using Zn||HP-P and Zn||AE symmetric cells (Fig. 2(k)). The current density in Zn||AE battery declined rapidly within 50 s and then tended to stable, indicating a two-dimensional (2D) diffusion of Zn^{2+} on Zn film and the accumulation of vertical Zn flakes as shown in Fig. 2(l) [15, 39]. Differently, in the Zn||HP-P anode, the current density only dropped slightly within 10 s and then rapidly managed by a stable and constant 3D diffusion process, suggesting the increasing number of Zn nucleation site and form a flat surface of Zn anode by the uniform and dense deposition of Zn-ion (Fig. 2(m)) [40].

3.3 Electrochemical performance of HP-P hydrogel electrolyte

To study the effect of HP-P structure on electrochemical characteristics, the CV between −0.2–0.6 V at scan rate of 0.1 mV·s^{-1} was firstly tested using SS||Zn half-cells with HP-P hydrogel electrolyte and aqueous electrolyte to reveal the positive role of HP-P electrolyte on Zn^{2+} deposition (Fig. 3(a)). The larger Zn deposition potential (−121 mV) of HP-P electrolyte negatively shifted compared with aqueous electrolyte (−78 mV). The larger nucleation overpotential is beneficial to form a smaller nucleus radius and uniform the Zn-deposition during deposition process [18, 41]. While the response current of HP-P electrolyte is smaller than that of aqueous electrolyte, which is mainly due to the low ionic conductivity (caused by the relatively low content of water in HP-P hydrogel) as displayed in Fig. S3 in the ESM. The electrochemical stability of HP-P hydrogel and aqueous electrolytes was explored by LSV and Tafel kinetics testing based on steel anode symmetrical cell (Figs. 3(b) and 3(c)). The LSV profiles show a lower potential for hydrogen evolution and higher potential for oxygen evolution of HP-P hydrogel electrolyte, indicating an increasing electrochemical stability [23, 42]. The more positive corrosion potential but higher corrosion current as shown in Tafel plots demonstrated that HP-P hydrogel electrolyte has a lower tendency of corrosion reactions than aqueous electrolyte, which is in good agreement with CV curves [17, 43].

To examine the structural advantages of the HP-P hydrogel electrolyte, symmetrical cells with hydrogel electrolyte (denoted as Zn||HP-P, Zn||HP, Zn||H_{99}P-P, Zn||H_{999}P-P) and AE (denoted as Zn||AE) were tested by galvanostatic cycling measurements at different currents and area capacities. Figure 3(d) shows the long-term symmetric cycling of the symmetrical cells with hydrogel electrolyte (HP-P, H_{99}P-P and H_{999}P-P) of different modulus at a current density of 0.5 mA·cm^{-2} and areal capacity of 0.5 mAh·cm^{-2}. The lifespan of Zn||HP-P hsymmetrical cell (4710) is much higher than that of Zn||H_{99}P-P (603 h) and Zn||H_{999}P-P (65 h) symmetrical cell, which further proves that the modulus of hydrogel electrolyte can effectively improve the reversibility and stability. The time–voltage plots of the Zn||HP-P symmetric cell display high consistency after 4000 h (Fig. S8 in the ESM), indicating the enhanced electrochemical stability of HP-P electrolyte. Compared with HP-P2, HP-P3, HP and AE symmetrical cell, the lifespan of HP-P symmetrical cell also has a clear advantage as displayed in Fig. 3(e) and Fig. S9 in the ESM. Notably, Zn||AE symmetrical cells have a lower voltage hysteresis than that of hydrogel electrolyte because of the higher ionic conductivity (Fig. S10 in the ESM), but a shorter lifespan than Zn||HP-P cells due to an uncontrolled dendrite.

Meanwhile, at higher current density of 1 and 2 mA·cm^{-2}, the HP-P electrolyte shows good reversibility (Fig. S11 in the ESM). The lifespan of Zn||HP-P symmetric cell reaches 2072 h at 1 mA·cm^{-2} and 940 h at 2 mA·cm^{-2}, which is much longer than Zn||HP and Zn||AE cells. It is worth mentioning that the HP-P electrolyte remains a good cycling stability and reversibility (1170 h at) as the increase of current density and capacity to 1 mA·cm^{-2} and 1 mAh·cm^{-2} (Figs. 3(f) and 3(g)). Figure 3(h) shows the rate performance of Zn||HP-P and Zn||AE symmetrical cells at constant areal capacity of 0.5 mAh·cm^{-2} and various current densities from 0.5 to 5 mA·cm^{-2}. The polarization voltage of Zn||HP-P symmetrical cell increases slightly as the increase of current density and falls back to the same level when the current density returns to 0.5 mA·cm^{-2}, demonstrating outstanding electrochemical cycle stability of the HP-P electrolyte. On the contrary, the polarization voltage of Zn||AE symmetrical cell becomes disturbed at 0.5 and 1 mA·cm^{-2} after large current density cycling (Fig. 3(i)).

The Coulombic efficiency (CE) of HP-P hydrogel and AE electrolyte using Zn||Cu half cell was shown in Fig. S12 in the ESM. The Coulombic efficiency of Zn||HP-P||Cu half-cell can remain at a

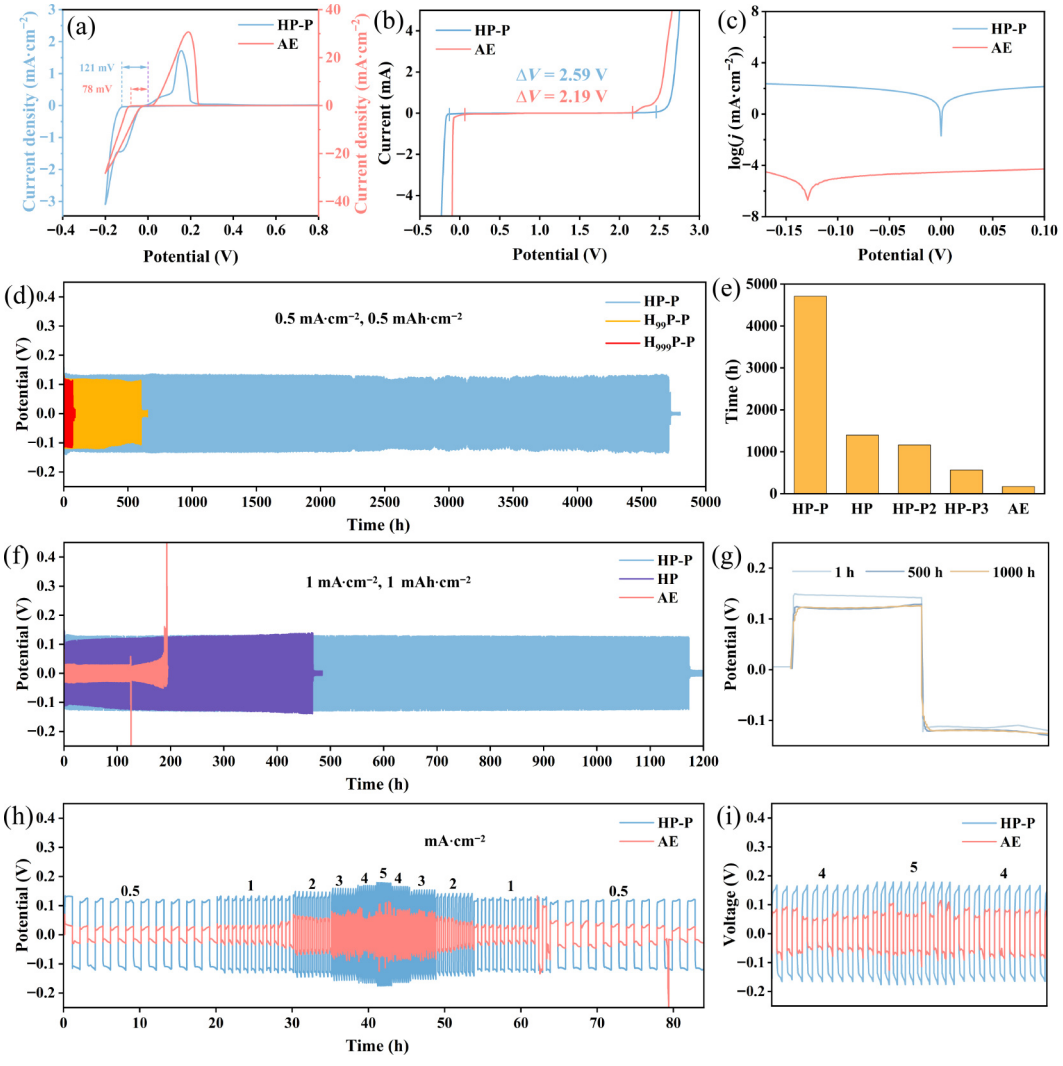

Figure 3 Electrochemical performance of the hydrogel electrolyte. (a) CV curves, (b) LSV profiles, and (c) linear polarization curves of HP-P and AE electrolyte. (d) Galvanostatic long-cycle data at 0.5 mA·cm^{-2} and 0.5 mAh·cm^{-2} of symmetrical cells with HP-P, H_{99}P-P and H_{999}P-P hydrogel electrolyte. (e) The comparison of lifespan of symmetrical cells with HP, HP-P2, HP-P3, and AE electrolyte. (f) and (g) Galvanostatic long-cycle data at 1 mA·cm^{-2} and 1 mAh·cm^{-2} with HP-P, HP and AE electrolytes. (h) and (i) Rate performances of Zn symmetric cells with HP-P and AE electrolytes.

high level of 99.8% after 140 cycles at 0.5 mA·cm^{-2} and 0.5 mAh·cm^{-2}, which is more stable than Zn||AE||Cu cell (declines rapidly to 70% after 20 cycles). Additionally, the charge/discharge voltage profiles from the 1st to 140th cycles are shown in Fig. S13 in the ESM. The Zn||Cu cell with HP-P electrolyte has a plating/stripping voltage hysteresis of 225 mV, which is higher than that of Zn||AE cell. The larger polarization voltage can promote the dense deposition of Zn and inhibit Zn-dendrite growth, which is in good agreement with the above-mentioned CV curves.

3.4 Electrochemical performance of NVO||HP-P||Zn full cell

To further demonstrate the possible practical application of HP-P electrolyte, full cells were assembled with NVO as cathode and Zn film as anode, HP-P hyrogel or Zn^{2+}-solution as electrolyte. The NVO nanobelts were prepared the same as the previously reported method [34]. The crystal information and morphology of NVO were verified by XRD and SEM (Fig. S14 in the ESM). All peaks in XRD pattern can be corresponded to the orthorhombic $NaV_3O_8{\cdot}1.5H_2O$ phase (PDF#16-0601). The NVO has a uniform nanobelts with a width of 300 nm and a length of 10 μm. The electrochemical performance of full cell is shown in Fig. 4. The CV was used to investigate the Zn-storage mechanism of NVO (Fig. 4(a)). Two distinct cathodic peaks at 0.79 and 1.03 V and the two anodic peaks at 0.51 and 0.75 V correspond to the insertion and disinsertion of Zn ions within the cathode, respectively [44]. The CV curves basically coincide from the second cycle to the fifth cycle, which shows the electrochemical stability of HP-P hydrogel electrolyte. The rate capabilities and galvanostatic charge/discharge curves of full cell with HP-P hydrogel electrolyte are displayed in Figs. 4(b) and 4(c). The HP-P electrolyte exhibits capacities of 388, 362, 318, 291, 265, 250 mAh·g^{-1} at 50, 100, 300, 500, 800, 1000 mA·g^{-1} and back to 376 mAh·g^{-1} at 50 mA·g^{-1} (Fig. 4(b)). Two well-defined discharge plateaus are in good agreement with CV curves and the well symmetric charge and discharge curves suggest an excellent reversibility of HP-P electrolyte (Fig. 4(c)).

The long-term cycling behavior of two batteries with HP-P hydrogel and Zn-salt aqueous electrolyte at 25 °C and current density of 0.5 and 1 A·g^{-1} are shown in Figs. 4(d) and 4(e), respectively. For the aqueous electrolyte full cell, the capacity fades

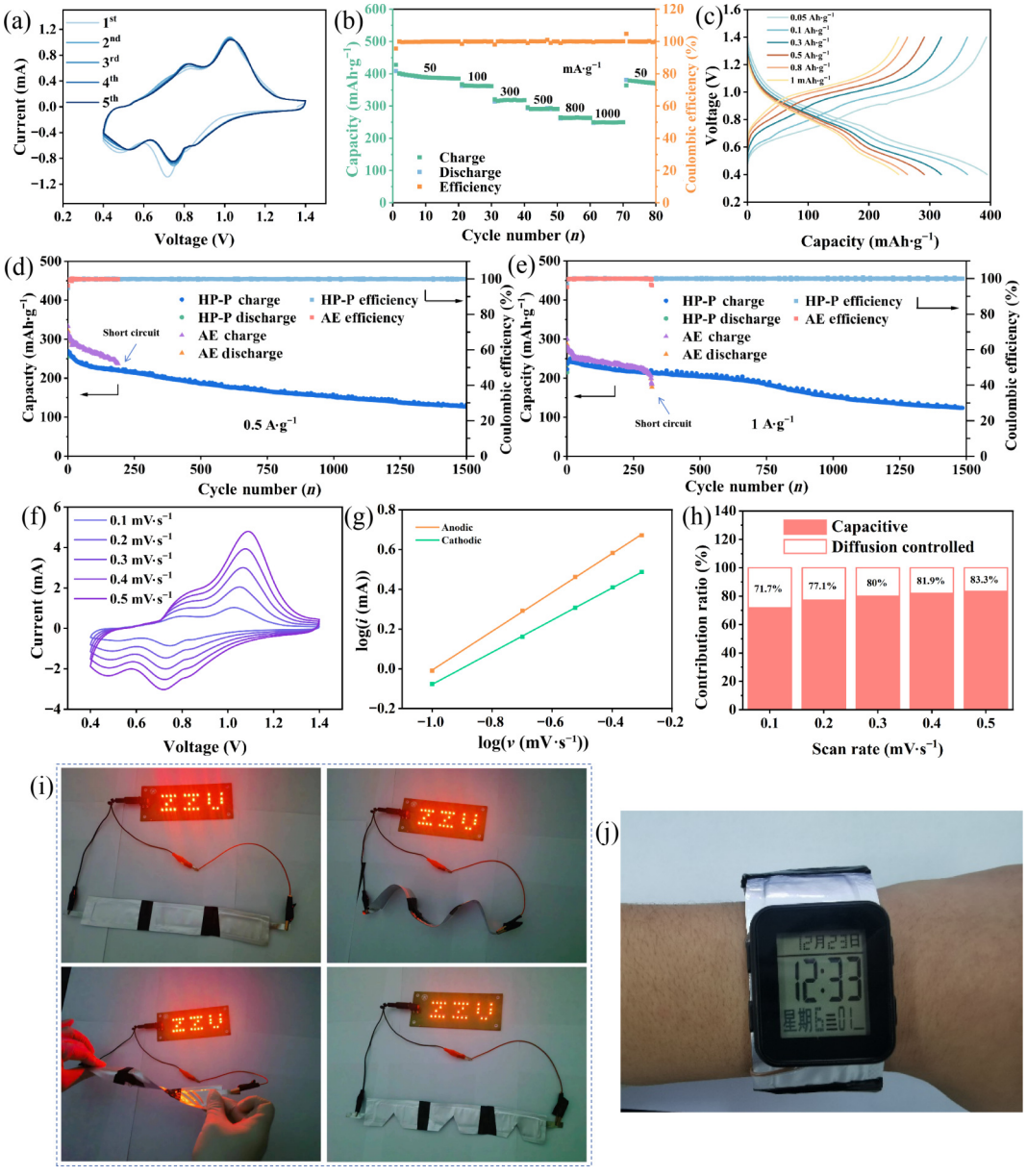

Figure 4 Zn-storage performance of the hydrogel electrolyte at room temperature. (a) CV curves at a scan rate of 0.5 mV·s^{-1}, (b) rate performances, and (c) specific capacity–voltage curves at different currents of Zn||NVO full cells. Discharge-specific capacity and CE (%) of Zn||NVO full cells with HP-P and AE electrolytes at (d) 0.5 A·g^{-1} and (e) 1 A·g^{-1}. (f) CV profiles at different scan rates, (g) the plots of log(i) versus log(v) at each redox-peak pair (peak current: i, scan rate: v), and (h) bar chart showing the percentages of pseudocapacitive contributions at different scan rates of Zn||HP-P||NVO full cells. Photographs of (i) LED lamp powered by Zn||HP-P||NVO full cell under bending, warping and cutting and (j) an electronic watch powered by strap-full-cells.

quickly and short circuit arises in hundreds of cycles at 0.5 and 1 A·g^{-1}. In comparison, the full cell with HP-P electrolyte has a high capacity of 131 mAh·g^{-1} after 1500 cycles. As the current density increase to 1 A·g^{-1}, the capacity remains 124 mAh·g^{-1} after 1500 cycles, indicating a good cycling stability of HP-P hydrogel. Figure 4(f) shows the CV profiles of Zn||NVO full cell with HP-P electrolyte at different scan rates from 0.1 to 0.5 mV·s^{-1} to calculate the contributions of the two different mechanisms (surface capacitive behavior and redox conversion) on specific capacity [45]. The plots of log(i) versus log(v) and the calculated percentages of pseudocapacitive contributions in the total capacity of NVO cathode are shown in Figs. 4(g) and 4(h), which is more evident capacitive-controlled as the increase of scan rate. The pouch battery employing HP-P hydrogel and flexible electrodes was fabricated to study the advances in flexibility (Fig. 4(i)). The flexible cell can power LED lamp under bending, warping and cutting without liquid leakage. Furthermore, a long battery pack made of three sets of cell in series can act as both a watch band and a power supply unit for an electronic watch (Fig. 4(j)).

The HP-P hydrogel has a good flexibility at −20 °C as mentioned above. To examine the electrochemical performance at low temperature of HP-P hydrogel, the voltage hysteresis was tested at different temperature (−20–60 °C) using Zn symmetrical cell (Fig. S15 in the ESM). The polarization increases as the temperature reduced to −20 °C, which is due to the activity of hydrogel electrolyte decreases at low temperature. The long-term symmetric cycling of the symmetrical cell at areal capacity of 0.5 mAh·cm^{-2} and current densities of 0.5 mA·cm^{-2} under operating temperature of

−20 °C are shown in Figs. 5(a) and 5(b). The lifespan can reach to 4000 h without the increasing of polarization, which is significantly exceeded the previously reported aqueous ZIBs (Table S1 in the ESM). Figures 5(c)–5(e) show the capacity and capacity–voltage of NVO||HP-P||Zn full cell at wide temperature range, which is 397, 360, 225, 224, 162, 112 mAh·g^{-1} at 60, 40, 20, 0, −10, −20 °C and back to the same capacity at the next cycle of temperature change, indicating the good reversibility and stability to fit for changes in temperature. The long-term charge/discharge cycling at −20 °C of NVO||HP-P||Zn full cell is displayed in Fig. 5(f). The capacity can keep at 66.4 mAh·g^{-1} (capacity retention ratio of 77%) after 10,000 cycles at current density of 0.5 A·g^{-1}, which shows higher stability and reversibility than the previously reported aqueous ZIBs (Table S2 in the ESM). It is worth noting that the increasing capacity in the initial cycles could be attributed as the activation process capacity [46, 47]. Normally, the activation process occurs under high current density (> 5 A·g^{-1}) [48]. The cathode needs more time to accommodate numerous Zn-ion ultrafast speed (de)insertion, leading to more active sites generated and the increasing capacity in the initial cycles [49]. In this work, the NVO cathode gets a low electrical activity at −20 °C, resulting in the activation process can occur at relative low current density. The pouch battery employing HP-P hydrogel can power an electronic watch (displays time, temperature and humidity) for 24 h at the operating temperature of −20 °C (Fig. 5(g)).

4 Conclusion

In summary, a kind of polyacrylate hydrogel electrolyte, the HP-P electrolyte, was fabricated in one step by UV curing method. The HP-P electrolyte displayed good mechanical property and freezing resistance. As electrolyte for ZIBs, the HP-P hydrogel electrolyte had an excellent reversibility and stability at various temperature. The Zn anode surface of symmetrical cell using the HP-P electrolyte remained smooth after 100 cycles, which due to the efficient adjustment on the dense and uniformed Zn-deposition. As

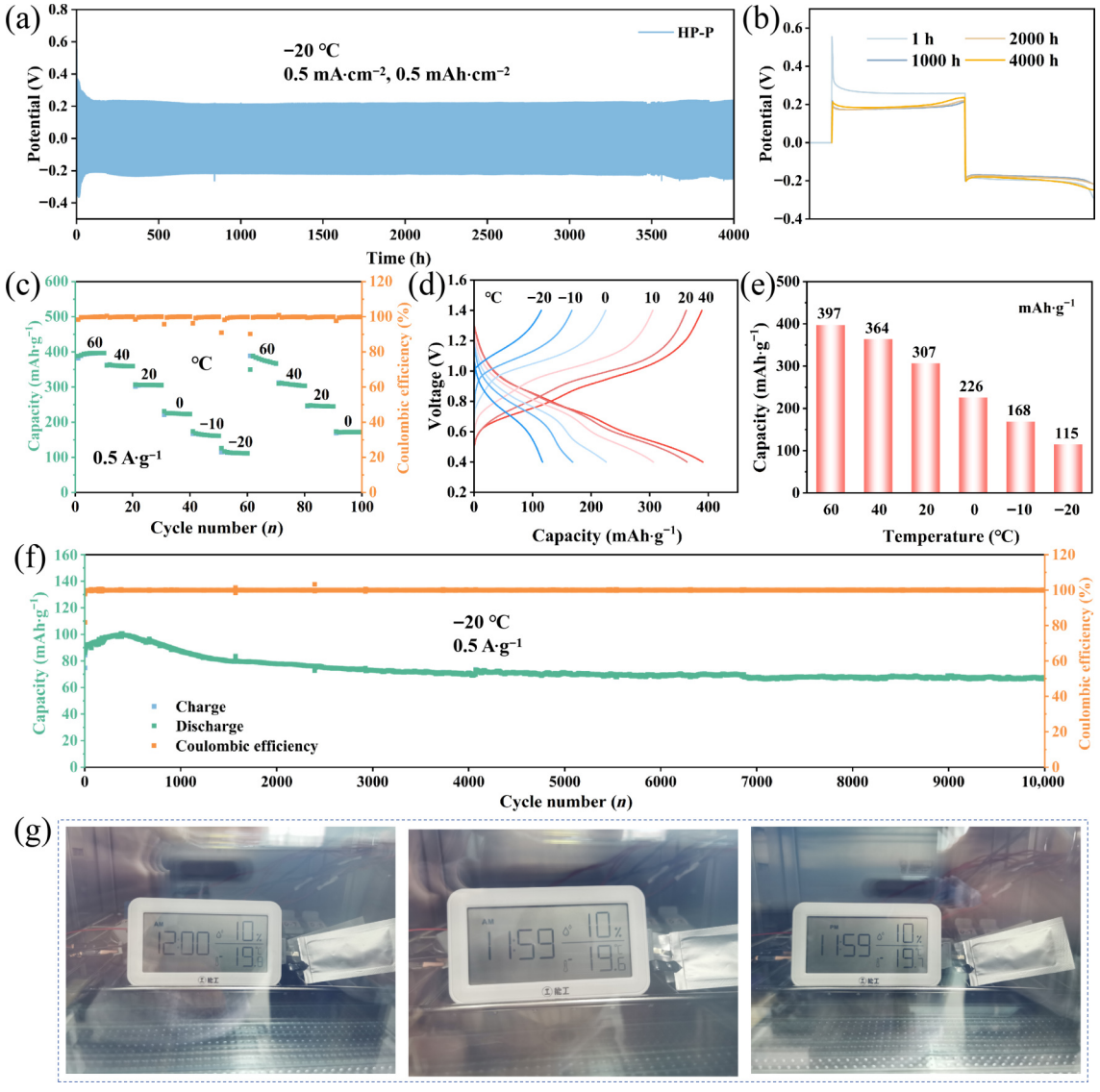

Figure 5 Zn-storage performance of the hydrogel electrolyte at low temperature. (a) Galvanostatic long-cycle data. (b) Localized long-term cycle curves at −20 °C of Zn||HP-P symmetric cell. (c) The capacity responsiveness under double cycle temperature change, (d) galvanostatic charge/discharge curves, and (e) capacity retention at wide temperature range from −20–60 °C. (f) Long-term cycling curves and Coulombic efficiency at −20 °C of NVO||HP-P||Zn full cells. (g) An electronic watch, with multifunction of time, temperature and humidity, powered by soft pack NVO||HP-P||Zn full battery.

a result, the symmetrical cell with HP-P electrolyte could run steadily for over 4710 and 4000 h at current density of 0.5 mA·cm^{-2} and areal capacity of 0.5 mAh·cm^{-2} under operating temperature of 25 and −20 °C, respectively. Meanwhile, the assembled full battery with NVO cathode and HP-P electrolyte had a high capacity of 131 mAh·g^{-1} after 1500 cycles and powered LED lamp under bending, warping and cutting without liquid leakage. Furthermore, the full battery showed a retention ratio of 77% after 10,000 cycles at current density of 0.5 A·g^{-1} and continuously powered an electronic watch under −20 °C.

Electronic Supplementary Material: Supplementary material (stress–strain curves and Young's modulus, SEM images, optical photographs, CLSM images, outline of Zn anode, galvanostatic long-cycle data, time–voltage plots, Coulombic efficiency) is available in the online version of this article at https://doi.org/10.26599/NR.2025.94906999.

Data availability

All data needed to support the conclusions in the paper are presented in the manuscript and/or the Electronic Supplementary Material. Additional data related to this paper may be requested from the corresponding author upon request.

Acknowledgements

The authors acknowledge the support from the National Natural Science Foundation of China (Nos. 52322708, 52377031 and 52002358), the National Natural Science Foundation of Henan (No. 242300421421) and State Key Laboratory of Advanced Electromagnetic Technology (No. AET 2023KF005).

Declaration of competing interest

All the contributing authors report no conflict of interests in this work.

Author contribution statement

Z. L. Z.: Data curation, project administration, validation, writing manuscript, experimental design. R. L. W., H. F. L., D. Z., and B. S.: Data curation, validation. Y. Z., J. X., and Y. J.: Project administration, funding acquisition, writing manuscript. All the authors have approved the final manuscript.

Use of AI statement

None.

References

[1] Zhang, Q.; Gao, X. W.; Liu, X.; Mu, J. J.; Gu, Q. F.; Liu, Z. M.; Luo, W. B. Flexible wearable energy storage devices: Materials, structures, and applications. *Batt. Energy.* **2024**, *3*, 20230061.

[2] Li, C. F.; Zhang, K.; Cheng, X. R.; Li, J. X.; Jiang, Y.; Li, P. Z.; Wang, B. J.; Peng, H. S. Polymers for flexible energy storage devices. *Prog. Polym. Sci.* **2023**, *143*, 101714.

[3] He, J. Y.; Cao, L. Q.; Cui, J. J.; Fu, G. W.; Jiang, R. Y.; Xu, X.; Guan, C. Flexible energy storage devices to power the future. *Adv. Mater.* **2024**, *36*, 2306090.

[4] Chen, S. Y.; Chen, Y. L.; Mu, X. J.; Wang, P. F.; Miao, L.; Tanemura, S.; Cai, H. F. Strategies for enhancing ionic conductivity and energy density of gel polymer electrolytes for next-generation flexible energy storage devices. *Sustain. Mater. Technol.* **2023**, *36*, e00635.

[5] Xiang, S. W.; Qin, L.; Wei, X. F.; Fan, X.; Li, C. M. Fabric-type flexible energy-storage devices for wearable electronics. *Energies* **2023**, *16*, 4047.

[6] Wang, D. H.; Han, C. P.; Mo, F. N.; Yang, Q.; Zhao, Y. W.; Li, Q.; Liang, G. J.; Dong, B. B.; Zhi, C. Y. Energy density issues of flexible energy storage devices. *Energy Stor. Mater.* **2020**, *28*, 264–292.

[7] Xu, Y. K.; Zhou, X.; Chen, Z. F.; Hou, Y.; You, Y.; Lu, J. Electrolyte formulas of aqueous zinc ion battery: A physical difference with chemical consequences. *Mater. Today* **2023**, *66*, 339–347.

[8] Shin, J.; Lee, J.; Park, Y.; Choi, J. W. Aqueous zinc ion batteries: Focus on zinc metal anodes. *Chem. Sci.* **2020**, *11*, 2028–2044.

[9] Kim, H. J.; Kim, S.; Heo, K.; Lim, J. H.; Yashiro, H.; Myung, S. T. Nature of zinc-derived dendrite and its suppression in mildly acidic aqueous zinc-ion battery. *Adv. Energy Mater.* **2023**, *13*, 2203189.

[10] Shang, Y.; Kundu, D. A path forward for the translational development of aqueous zinc-ion batteries. *Joule* **2023**, *7*, 244–250.

[11] Li, G. J.; Sun, L.; Zhang, S. L.; Zhang, C. F.; Jin, H. Y.; Davey, K.; Liang, G. M.; Liu, S. L.; Mao, J. F.; Guo, Z. P. Developing cathode materials for aqueous zinc ion batteries: Challenges and practical prospects. *Adv. Funct. Mater.* **2024**, *34*, 2301291.

[12] Zhu, J. C.; Tie, Z. W.; Bi, S. S.; Niu, Z. Q. Towards more sustainable aqueous zinc-ion batteries. *Angew. Chem., Int. Ed.* **2024**, *136*, e202403712.

[13] Zhang, Y. S.; Khademhosseini, A. Advances in engineering hydrogels. *Science* **2017**, *356*, aaf3627.

[14] Vandeginste, V.; Wang, J. R. A review of the synthesis of biopolymer hydrogel electrolytes for improved electrode–electrolyte interfaces in zinc-ion batteries. *Energies* **2024**, *17*, 310.

[15] Yang, Y.; Hua, H. M.; Lv, Z. H.; Meng, W. W.; Zhang, M. H.; Li, H.; Lin, P. X.; Yang, J.; Chen, G. H.; Kang, Y. H. et al. Diminishing space-charge layer effect of zinc anodes by an anion-immobilized electrolyte membrane. *ACS Energy Lett.* **2023**, *8*, 1959–1968.

[16] Wang, Y. B.; Li, Q.; Hong, H.; Yang, S.; Zhang, R.; Wang, X. Q.; Jin, X.; Xiong, B.; Bai. S.; Zhi. C. Y. Lean-water hydrogel electrolyte for zinc ion batteries. *Nat. Commun.* **2023**, *14*, 3890.

[17] Ji, S. G.; Qin, J. X.; Yang, S. S.; Shen, P.; Hu, Y. Y.; Yang, K.; Luo, H.; Xu, J. A mechanically durable hybrid hydrogel electrolyte developed by controllable accelerated polymerization mechanism towards reliable aqueous zinc-ion battery. *Energy Stor. Mater.* **2023**, *55*, 236–243.

[18] Lin, P. X.; Chen, G. H.; Kang, Y. H.; Zhang, M. H.; Yang, J.; Lv, Z. H.; Yang, Y.; Zhao, J. B. Simultaneous inhibition of Zn dendrites and polyiodide ions shuttle effect by an anion concentrated electrolyte membrane for long lifespan aqueous zinc-iodine batteries. *ACS Nano* **2023**, *17*, 15492–15503.

[19] Ma, R. J.; Xu, Z. X.; Wang. X. L. Polymer hydrogel electrolytes for flexible and multifunctional zinc-ion batteries and capacitors. *Energy Environ. Mater.* **2023**, *6*, e12464.

[20] Yuan, C. M.; Zhong, X.; Tian, P. S.; Wang, Z.; Gao, G. H.; Duan, L. F.; Wang, C. S.; Shi, F. W. Antifreezing zwitterionic-based hydrogel electrolyte for aqueous Zn ion batteries. *ACS Appl. Energy Mater.* **2022**, *5*, 7530–7537.

[21] Chen, M. H.; Xie, S. A.; Zhao, X. Y.; Zhou, W. H.; Li, Y.; Zhang, J. W.; Chen, Z.; Chao, D. L. Aqueous zinc-ion batteries at extreme temperature: Mechanisms, challenges, and strategies. *Energy Stor. Mater.* **2022**, *51*, 683–718.

[22] Mo, F. N.; Cui, M. W.; He, N.; Chen, L. N.; Fei, J. B.; Ma, Z. Y.; Yu, S. Z.; Wei, J.; Huang, Y. Recent progress and perspectives on advanced flexible Zn-based batteries with hydrogel electrolytes. *Mater. Res. Lett.* **2022**, *10*, 501–520.

[23] Li, X. Y.; Wang, D. H.; Ran, F. Key approaches and challenges in fabricating advanced flexible zinc-ion batteries with functional hydrogel electrolytes. *Energy Stor. Mater.* **2023**, *56*, 351–393.

[24] Wang, D. H.; Li, H. F.; Liu, Z. X.; Tang, Z. J.; Liang, G. J.; Mo, F. N.;

Yang, Q.; Ma, L. T.; Zhi, C. Y. A nanofibrillated cellulose/polyacrylamide electrolyte-based flexible and sewable high-performance Zn–MnO_2 battery with superior shear resistance. *Small* **2018**, *14*, 1803978.

[25] Hu, Y. Q.; Wang, Z.; Li, Y. Z.; Liu, P. W.; Liu, X. L.; Liang, G. X.; Zhang, D.; Fan, X.; Lu, Z. G.; Wang, W. X. Sulfonated hydrogel electrolyte enables dendrite-free zinc-ion batteries. *Chem. Eng. J.* **2024**, *479*, 147762.

[26] Shi, Y.; Wang, R.; Bi, S. S.; Yang, M.; Liu, L. L.; Niu, Z. Q. An anti-freezing hydrogel electrolyte for flexible zinc-ion batteries operating at −70 °C. *Adv. Funct. Mater.* **2023**, *33*, 2214546.

[27] Huang, S. W.; Hou, L.; Li, T. Y.; Jiao, Y. C.; Wu, P. Y. Antifreezing hydrogel electrolyte with ternary hydrogen bonding for high-performance zinc-ion batteries. *Adv. Mater.* **2022**, *34*, 2110140.

[28] Yan, Y. C.; Duan, S. D.; Liu, B.; Wu, S. W.; Alsaid, Y.; Yao, B. W.; Nandi, S.; Du, Y. J.; Wang, T. W.; Li, Y. Z. et al. Tough hydrogel electrolytes for anti-freezing zinc-ion batteries. *Adv. Mater.* **2023**, *35*, 2211673.

[29] Sun, T. J.; Yuan, X. M.; Wang, K.; Zheng, S. B.; Shi, J. Q.; Zhang, Q.; Cai, W. S.; Liang, Jing.; Tao, Z. L. An ultralow-temperature aqueous zinc-ion battery. *J. Mater. Chem. A* **2021**, *9*, 7042–7047.

[30] Hu, F. L.; Li, M. Y.; Gao, G. W.; Fan, H. Q.; Ma, L. T. The gel-state electrolytes in zinc-ion batteries. *Batteries* **2022**, *8*, 214.

[31] Zhao, S. Y.; Zuo, Y. Y.; Liu, T.; Zhai, S.; Dai, Y. W.; Guo, Z. J.; Wang, Y.; He, Q. J.; Xia, L. C.; Zhi, C. Y. et al. Multi-functional hydrogels for flexible zinc-based batteries working under extreme conditions. *Adv. Energy Mater.* **2021**, 11. 2101749.

[32] Bu, F.; Gao, Y.; Wang, Q. Z.; Wang, Y. X.; Li, C.; Yang, J. Y.; Liu, X. Y.; Guan, C. Ultraviolet-assisted printing of flexible solid-state Zn-ion battery with a heterostructure electrolyte. *Small* **2023**, *19*, 2303108.

[33] Bu, F.; Li, C.; Wang, Q. Z.; Liu, X. Y. Ultraviolet-assisted printing of flexible all-solid-state zinc batteries with enhanced interfacial bond. *Chem. Eng. J.* **2022**, *449*, 137710.

[34] Wan, F.; Zhang, L. L.; Dai, X.; Wang, X. Y.; Niu, Z. Q.; Chen, J. Aqueous rechargeable zinc/sodium vanadate batteries with enhanced performance from simultaneous insertion of dual carriers. *Nat. Commun.* **2018**, *9*, 1656.

[35] Meng, Y.; Zhang, L. F.; Peng, M. J.; Shen, D. N.; Zhu, C. H.; Qian, S. Y.; Liu, J.; Cao, Y. F.; Yan, C. L.; Zhou, J. Q. et al. Developing thermoregulatory hydrogel electrolyte to overcome thermal runaway in zinc-ion batteries. *Adv. Funct. Mater.* **2022**, *32*, 2206653.

[36] Lu, H. F.; Zhang, D.; Jin, Q. Z.; Zhang, Z. L.; Lyu, N. W.; Zhu, Z. J.; Duan, C. X.; Qin, Y.; Jin, Y. Gradient electrolyte strategy achieving long-life zinc anodes. *Adv. Mater.* **2023**, *35*, 2300620.

[37] Wei, T. T.; Ren, Y. K.; Li, Z. Q.; Zhang, X. X.; Ji, D. H.; Hu, L. H. Bonding interaction regulation in hydrogel electrolyte enable dendrite-free aqueous zinc-ion batteries from −20 to 60 °C. *Chem. Eng. J.* **2022**, *434*, 134646.

[38] Xiong, T.; Zhang, D. Q.; Yeo, J. Y.; Zhan, Y. F.; Ong, Y. K.; Limpo, C. M. A.; Shi, L.; Rao, Y. F.; Pu, Y. H.; Lai, W. H. et al. Interfacial design towards stable zinc metal-free zinc-ion batteries with high energy density. *J. Mater. Chem. A* **2024**, *12*, 5499–5507.

[39] Xiang, Z. P.; Li, Y. Y.; Cheng, X. J.; Yang, C.; Wang, K. P.; Zhang, Q.; Wang, L. Lean-water hydrogel electrolyte with improved ion conductivity for dendrite-free zinc-ion batteries. *Chem. Eng. J.* **2024**, *490*, 151524.

[40] Lu, H. Y.; Hu, J. S.; Wei, X. J.; Zhang, K. Q.; Xiao, X.; Zhao, J. X.; Hu, Q.; Yu, J.; Zhou, G. M.; Xu, B. G. A recyclable biomass electrolyte towards green zinc-ion batteries. *Nat. Commun.* **2023**, *14*, 4435.

[41] Zhang, H. D.; Gan, X. T.; Yan, Y. Y.; Zhou, J. P. A sustainable dual cross-linked cellulose hydrogel electrolyte for high-performance zinc-metal batteries. *Nano-Micro Lett.* **2024**, *16*, 106.

[42] Lu, H. Y.; Hu, J. S.; Wang, L. T.; Li, J. Z.; Ma, X.; Zhu, Z. C.; Li, H. Q.; Zhao, Y. J.; Li, Y. J.; Zhao, J. X. et al. Multi-component crosslinked hydrogel electrolyte toward dendrite-free aqueous Zn ion batteries with high temperature adaptability. *Adv. Funct. Mater.* **2022**, *32*, 2112540.

[43] Gu, Y.; Zheng, X. W.; Zhou, Z.; Chen, G. X.; Chen, S. M.; Li, Q. F. Amphiphilic ionic liquid hydrogel electrolytes with high ionic conductivity towards dendrite-free ultra-stable aqueous zinc ion batteries. *J. Energy Storage* **2024**, *89*, 111892.

[44] Lv, Y. Q.; Zhao, M.; Du, Y. D.; Kang, Y.; Xiao, Y.; Chen, S. M. Engineering a self-adaptive electric double layer on both electrodes for high-performance zinc metal batteries. *Energy Environ. Sci.* **2022**, *15*, 4748–4760.

[45] Qin, M. L.; Zhang, Z. L.; Zhao, Y. Z.; Liu, L.; Jia, B. R.; Han, K.; Wu, H. Y.; Liu, Y.; Wang, L. J.; Min, X. et al. Optimization of von mises stress distribution in mesoporous α-Fe_2O_3/C hollow bowls synergistically boosts gravimetric/volumetric capacity and high-rate stability in alkali-ion batteries. *Adv. Funct. Mater.* **2019**, *29*, 1902822.

[46] Islam, S.; Lee, S.; Lee, S.; Hilmy Alfaruqi, M.; Sambandam, B.; Mathew, V.; Hwang, J. Y.; Kim, J. Triggering the theoretical capacity of $Na_{1.1}V_3O_{7.9}$ nanorod cathode by polypyrrole coating for high-energy zinc-ion batteries. *Chem. Eng. J.* **2022**, *446*, 137069.

[47] He, P.; Zhang, G. B.; Liao, X. B.; Yan, M. Y.; Xu, X.; An, Q. Y.; Liu, J.; Mai, L. Q. Sodium ion stabilized vanadium oxide nanowire cathode for high-performance zinc-ion batteries. *Adv. Energy Mater.* **2018**, *8*, 1702463.

[48] Soundharrajan, V.; Sambandam, B.; Kim, S.; Alfaruqi, M. H.; Putro, D. Y.; Jo, J.; Kim, S.; Mathew, V.; Sun, Y. K.; Kim, J. $Na_2V_6O_{16}{\cdot}3H_2O$ barnesite nanorod: An open door to display a stable and high energy for aqueous rechargeable Zn-ion batteries as cathodes. *Nano Lett.* **2018**, *18*, 2402–2410.

[49] She, B. H.; Shan, L. T.; Chen, H. J.; Zhou, J.; Guo, X.; Fang, G. Z.; Cao, X. X.; Liang, S. Q. Investigation of sodium vanadate as a high-performance aqueous zinc-ion battery cathode. *J. Energy Chem.* **2019**, *37*, 172–175.